

## Exceptional Points in Quasinormal Spectra of Hairy Black Holes

Lang Cheng<sup>a,\*</sup>, Xiaobo Guo<sup>b,†</sup>, Yuhan Li<sup>a,‡</sup>, Jun Tao<sup>a,§</sup> and Peng Wang<sup>a,¶</sup>

<sup>a</sup>*College of Physics, Sichuan University, Chengdu, 610065, China and*

<sup>b</sup>*School of Data Science, Shanghai University of Finance  
and Economics Zhejiang College, Jinhua, 321015, China*

Exceptional points (EPs) in quasinormal mode (QNM) spectra are non-Hermitian degeneracies at which both the eigenvalues and eigenfunctions coalesce. In this paper, we identify an EP in the scalar QNM spectrum of hairy black holes in the Einstein-Maxwell-scalar theory by scanning the parameter space. We then investigate its implications for ringdown signals by extracting QNMs from time-domain waveforms. Our results show that an EP ansatz, which includes a resonant contribution containing a term linear in time, provides a more robust description of ringdown at the EP than the standard ansatz based on a superposition of independent damped modes. In particular, it captures the resonant contribution associated with spectral coalescence more naturally and enables a more reliable extraction from the ringdown signal.

arXiv:2603.22261v1 [gr-qc] 23 Mar 2026

---

\* [langcheng@stu.scu.edu.cn](mailto:langcheng@stu.scu.edu.cn)

† [guobo@ustc.edu.cn](mailto:guobo@ustc.edu.cn)

‡ [leeyhan@stu.scu.edu.cn](mailto:leeyhan@stu.scu.edu.cn)

§ [taojun@scu.edu.cn](mailto:taojun@scu.edu.cn)

¶ [pengw@scu.edu.cn](mailto:pengw@scu.edu.cn)

## CONTENTS

I. Introduction		2
II. Setup		4
A. Black Hole Solution		4
B. Scalar QNM		5
C. Waveform Extraction		7
III. QNM Spectrum		8
IV. QNM Extraction		11
A. Weak Fit		12
B. Strong Fit		14
V. Conclusion		17
Acknowledgments		18
References		18

## I. INTRODUCTION

The ringdown stage of a perturbed black hole (BH) is governed by its quasinormal modes (QNMs), whose complex frequencies determine the oscillation rates and damping times of the spacetime response. QNMs therefore play a central role in BH spectroscopy and provide a direct link between gravitational-wave (GW) observations and the properties of compact objects [1–5]. In the standard description, the ringdown signal is written as a superposition of exponentially damped modes. A basic issue, however, is how reliably these modes can be identified and extracted from time-domain waveforms, especially when several modes contribute at comparable levels or when the relevant frequencies are nearly degenerate [6–8].

Recent developments have highlighted the non-Hermitian character of the QNM eigenvalue problem. Because QNMs are defined by purely ingoing boundary conditions at the horizon and purely outgoing boundary conditions at spatial infinity, the resulting spectral problem is intrinsically non-Hermitian [9–11]. As a result, the spectrum can display pronounced sensitivity to perturbations, pseudospectral broadening, resonance, and other effects familiar from non-Hermitian theory [12–

20]. Among these, exceptional points (EPs) have attracted increasing attention in BH perturbation theory, especially with the advent of high-precision GW astronomy [21–25]. An EP is a spectral degeneracy at which two eigenvalues and their associated eigenfunctions coalesce [26–34]. Near such a point, the spectrum develops the characteristic square-root branch structure, which is associated with a variety of phenomena, including mode switching, hysteresis, and resonant behavior [35–37].

EPs generally require a parameter space of dimension greater than one. A representative example is provided by massive scalar perturbations of Kerr BHs, where EPs appear in the parameter space spanned by the BH spin and the scalar mass [35, 38–41]. A related construction can also be realized by adding a Gaussian bump to the curvature effective potential that governs BH perturbations, and this idea has recently been extended from isolated EPs to continuous exceptional lines [36, 42, 43]. By contrast, when only a restricted one-parameter scan is available, an exact EP is generically replaced by mode repulsion or an avoided crossing, which can be understood as the one-dimensional trace of a nearby EP in a higher-dimensional parameter space [44–52].

These features matter not only for the organization of the QNM spectrum in the frequency domain, but also for the description of ringdown signals in the time domain. Near an EP, the usual expansion in terms of independent exponentially damped QNMs is modified by a resonant contribution containing both an exponential factor and a term linear in time [36]. Consequently, the presence of an EP can leave a characteristic imprint on the waveform and affect the extraction and interpretation of ringdown signals. Recent studies have also indicated that an EP based description can capture near resonant BH ringdown more naturally than the standard superposition of independent damped modes [37, 53].

Most existing studies of EPs in BH perturbation theory have focused on BHs satisfying the no-hair theorem, whereas the corresponding problem in hairy BH backgrounds remains much less explored. This naturally raises the question of whether similar non-Hermitian structures also arise in BH solutions with nontrivial hair. In particular, hairy BHs in the Einstein-Maxwell-scalar (EMS) theory provide a useful setting in which to investigate this issue. The theory admits asymptotically flat BH solutions with scalar hair and contains two independent control parameters, allowing for a richer spectral structure [54–65]. More importantly, recent studies of the scalar QNM spectrum of EMS hairy BHs have identified two distinct families of modes with different spectral stability properties: peak modes, which are localized near the potential peak and are associated with the photon sphere, and off-peak modes, which are localized away from the potential peak and retain an imprint of the valley structure arising in the double-peaked effective potential [66]. An avoided

crossing between a peak mode branch and an off-peak mode branch was also observed, suggesting that an EP may emerge once the full two-parameter space is explored.

In this paper, we study EPs in the scalar QNM spectrum of hairy BHs in the EMS model and investigate their implications for ringdown signals. Specifically, we identify an EP in the QNM spectrum and compare the corresponding time-domain extraction using the standard QNM ansatz and an EP based ansatz. The remainder of this paper is organized as follows. In Sec. II, we briefly review the background hairy BH solutions and the numerical framework. In Sec. III, we present the QNM spectrum and discuss the EP structure. In Sec. IV, we analyze the corresponding ringdown signal and its extraction. We conclude in Sec. V with a summary and discussion. Throughout this work, we employ geometrized units with  $G = c = 1$ .

## II. SETUP

In this section, we outline the background BH solutions and the framework used to compute the QNM spectrum of a test scalar field. We also summarize our numerical strategy, including both the frequency-domain spectral method and the time-domain waveform extraction.

### A. Black Hole Solution

We study the scalar QNM spectrum of static, spherically symmetric BH backgrounds in the Einstein-Maxwell-scalar (EMS) theory. The theory contains a real scalar field  $\phi$  that is minimally coupled to the spacetime metric and nonminimally coupled to the electromagnetic field  $A_\mu$ . The dynamics is governed by the action [55]

$$S = \int d^4x \sqrt{-g} \left[ R - 2(\partial\phi)^2 - e^{\alpha\phi^2} F^{\mu\nu} F_{\mu\nu} \right], \quad (1)$$

where  $F_{\mu\nu} = \partial_\mu A_\nu - \partial_\nu A_\mu$  is the electromagnetic field strength tensor. The coupling function  $e^{\alpha\phi^2}$  encodes the interaction between  $\phi$  and  $A_\mu$ , where  $\alpha$  denotes the coupling constant.

Within this framework, the equations of motion admit static, spherically symmetric, asymptotically flat BH solutions endowed with nontrivial scalar hair. Adopting the metric ansatz

$$ds^2 = -N(r) e^{-2\delta(r)} dt^2 + \frac{dr^2}{N(r)} + r^2 d\Omega^2, \quad (2)$$

together with the electrostatic potential  $A_\mu dx^\mu = \Phi(r) dt$ , the equations of motion reduce to a set

of four coupled ordinary differential equations for the functions  $N(r)$ ,  $\delta(r)$ ,  $\phi(r)$ , and  $\Phi(r)$ :

$$\begin{aligned}
N'(r) &= \frac{1 - N(r)}{r} - \frac{Q^2}{r^3 e^{\alpha\phi^2(r)}} - rN(r) [\phi'(r)]^2, \\
[r^2 N(r) \phi'(r)]' &= -\frac{\alpha Q^2 \phi(r)}{r^2 e^{\alpha\phi^2(r)}} - r^3 N(r) [\phi'(r)]^3, \\
\delta'(r) &= -r [\phi'(r)]^2, \\
\Phi'(r) &= \frac{Q}{r^2 e^{\alpha\phi^2(r)}} e^{-\delta(r)},
\end{aligned} \tag{3}$$

where  $Q$  is the electric charge, and primes denote derivatives with respect to the areal radius  $r$ . Regularity at the event horizon and asymptotic flatness at spatial infinity fix the boundary conditions. Owing to a scaling symmetry of the field equations, the family of solutions can be parameterized by the dimensionless pair  $(\alpha, q)$ , where  $q \equiv Q/M$ , and  $M$  denotes the ADM mass of the BH. Following [66], we construct the hairy BH solutions using a spectral method.

The hairy BH solutions considered here are also referred to as scalarized Reissner-Nordström (RN) BHs. In the EMS theory, the nonminimal coupling between the scalar and electromagnetic fields can trigger a tachyonic instability, so that an originally bald RN BH can dynamically evolve into a scalarized BH. Studying the dynamical properties of these scalarized BHs therefore provides a useful window into the mechanism of spontaneous scalarization [67–74]. In addition, the scalarized BHs can exhibit multiple light rings in the equatorial plane [75, 76], leading to distinctive optical signatures in BH imaging [77–81].

## B. Scalar QNM

For simplicity, we consider a test, massless, neutral scalar field  $\Psi$  propagating on the hairy BH background. In the test field approximation,  $\Psi$  is assumed to be sufficiently weak that its backreaction on the background spacetime can be neglected. The scalar field  $\Psi$  obeys the Klein-Gordon equation

$$\frac{1}{\sqrt{-g}} \partial_\mu (g^{\mu\nu} \sqrt{-g} \partial_\nu \Psi) = 0. \tag{4}$$

Exploiting the spherical symmetry of the background spacetime, we decompose the scalar field as

$$\Psi(t, r, \theta, \varphi) = \frac{1}{r} \sum_{l,m} \psi_{lm}(t, r) Y_{l,m}(\theta, \varphi). \tag{5}$$

Substituting this decomposition into Eq. (4), we obtain a one-dimensional Regge-Wheeler-Zerilli-type wave equation,

$$\left( -\frac{\partial^2}{\partial t^2} + \frac{\partial^2}{\partial r^{*2}} - V_{\text{eff}}(r) \right) \psi(t, r) = 0, \tag{6}$$

where the tortoise coordinate  $r^*$  is defined by

$$\frac{dr^*}{dr} \equiv \frac{e^{\delta(r)}}{N(r)}, \quad (7)$$

and the effective potential is

$$V_{\text{eff}}(r) = \frac{e^{-2\delta(r)}N(r)}{r^2} \left[ l(l+1) + 1 - N(r) - \frac{Q^2}{r^2 e^{\alpha\phi^2(r)}} \right]. \quad (8)$$

Here  $l$  is the angular quantum number.

To obtain the QNM spectrum, we work in the frequency domain by Fourier decomposing

$$\psi(t, r) = \int d\omega \tilde{\psi}(\omega, r) e^{-i\omega t}, \quad (9)$$

which yields the frequency-domain master equation

$$\left( \frac{d^2}{dr^{*2}} + \omega^2 - V_{\text{eff}}(r) \right) \tilde{\psi}(\omega, r) = 0. \quad (10)$$

The QNM frequencies  $\omega$  are determined by imposing purely ingoing boundary conditions at the event horizon ( $r = r_H$ ) and purely outgoing conditions at spatial infinity ( $r \rightarrow \infty$ ). From the asymptotic analysis, the wave function behaves as

$$\begin{aligned} \tilde{\psi}(\omega, r) &\sim (r - r_H)^{-i\omega/\sqrt{f_H h_H}}, & r \rightarrow r_H, \\ \tilde{\psi}(\omega, r) &\sim e^{i\omega r} (r/r_H)^{-i(f_I+h_I)\omega/2}, & r \rightarrow \infty. \end{aligned} \quad (11)$$

The coefficients  $f_H$ ,  $h_H$ ,  $f_I$ , and  $h_I$  follow from the near-horizon and asymptotic expansions of the metric functions,

$$\begin{aligned} N(r) e^{-2\delta(r)} &\sim f_H (r - r_H), & N(r) &\sim h_H (r - r_H), \\ N(r) e^{-2\delta(r)} &\sim 1 + f_I/r, & N(r) &\sim 1 + h_I/r, \end{aligned} \quad (12)$$

where the second line holds for  $r \rightarrow \infty$ . For stable QNMs with  $\text{Im}(\omega) < 0$ , the corresponding solutions diverge at both the horizon and spatial infinity. To facilitate the numerical computation, we therefore factor out the known asymptotic behavior by writing

$$\tilde{\psi}(\omega, r) = e^{i\omega r} (r/r_H)^{-i\frac{(f_I+h_I)\omega}{2}} (1 - r_H/r)^{-\frac{i\omega}{\sqrt{f_H h_H}}} u(r). \quad (13)$$

Substituting this ansatz into Eq. (10) yields an ordinary differential equation for  $u(r)$ .

To carry out the numerical computation, we introduce the compactified radial coordinate  $x = 1 - 2r_H/r$ , which maps  $r \in [r_H, \infty)$  to  $x \in [-1, 1]$ . In this coordinate, the function  $u(x)$  is approximated by a truncated Chebyshev spectral expansion,

$$u(x) \simeq \sum_{n=0}^{N_x-1} c_n T_n(x), \quad (14)$$

where  $c_n$  are the spectral coefficients,  $T_n(x)$  are the Chebyshev polynomials of the first kind, and  $N_x$  denotes the number of collocation points, i.e., the spectral resolution. Evaluating the differential equation for  $u(x)$  at the Chebyshev collocation points yields a set of  $N_x$  coupled algebraic equations for the  $N_x$  unknown coefficients  $c_n$ . To remove the linear scaling invariance of Eq. (10), we impose a normalization condition by fixing  $u(-1) = 1$ . This provides one additional algebraic constraint. To maintain a square system, we treat the QNM frequency  $\omega$  as an additional unknown, so that the total number of equations matches the total number of variables.

The resulting nonlinear algebraic system for  $\{c_n\}$  and  $\omega$  is solved in the complex plane using the Newton-Raphson method. Starting from an initial guess, each iteration linearizes the residual equations around the current estimate and updates the solution by solving the associated linear system for the correction. In our implementation, the linear system at each step is solved with the built-in `LinearSolve` function in MATHEMATICA. The iteration is terminated when the difference between successive iterates falls below  $10^{-10}$ , indicating numerical convergence.

### C. Waveform Extraction

Alternatively, the QNMs of the scalar field  $\Psi$  can be extracted from its time-domain waveform. The waveform is obtained by numerically integrating Eq. (6) with a second-order leapfrog method. Defining  $\psi_{i,j} \equiv \psi(i\Delta t, j\Delta r^*)$  and  $V_j \equiv V_{\text{eff}}(j\Delta r^*)$ , the evolution is implemented via

$$\psi_{i+1,j} = -\psi_{i-1,j} + \frac{\Delta t^2}{\Delta r^{*2}} (\psi_{i,j+1} + \psi_{i,j-1} - 2\psi_{i,j}) - \Delta t^2 V_j \psi_{i,j}. \quad (15)$$

We choose  $\Delta t/\Delta r^* = 1/2$  to ensure numerical stability. The initial data are specified as a Gaussian pulse centered near the peak of the effective potential,

$$\psi(t = 0, r^*) = \exp\left[-\frac{(r^* - a)^2}{2\sigma^2}\right], \quad (16)$$

where  $a$  denotes the peak location, and we set  $\psi(t < 0, r^*) = 0$ .

It is well known that the late-time waveform can be approximated as a superposition of  $N$  exponentially damped sinusoids associated with individual QNMs,

$$\psi(t) \simeq \text{Re} \sum_{n=0}^{N-1} A_n e^{-i(\omega_n t - \phi_n)}. \quad (17)$$

Here  $\omega_n$ ,  $A_n$ , and  $\phi_n$  are the frequency, amplitude, and phase of the  $n$ th mode, respectively. However, when two QNMs coalesce at an EP, the QNM expansion is modified to [37]

$$\psi(t) \simeq \text{Re} \sum_{n \neq \text{EP}} A_n e^{-i(\omega_n t - \phi_n)} + \text{Re} \left[ \left( A_0^{\text{EP}} e^{i\phi_0^{\text{EP}}} + A_1^{\text{EP}} e^{i\phi_1^{\text{EP}}} t \right) e^{-i\omega_{\text{EP}} t} \right], \quad (18)$$

where  $\omega_{\text{EP}}$  denotes the QNM frequency at the EP. The coefficients  $A_0^{\text{EP}}$  and  $A_1^{\text{EP}}$  characterize the time-independent and linearly time-dependent contributions, respectively, while  $\phi_0^{\text{EP}}$  and  $\phi_1^{\text{EP}}$  are the corresponding phases. In the following, when extracting QNMs via waveform fitting, we refer to the ansatzes in Eqs. (17) and (18) as the standard and EP ansatzes, respectively. In addition, for the  $n$ th peak (off-peak) mode, the corresponding frequency, amplitude, and phase are denoted by  $\omega_n^p$ ,  $A_n^p$ , and  $\phi_n^p$  ( $\omega_n^o$ ,  $A_n^o$ , and  $\phi_n^o$ ), respectively.

We employ two fitting schemes to extract QNMs from the time-domain waveform: (i) *Strong (agnostic) fit*: all parameters are treated as free, and we use the `NonlinearModelFit` function in MATHEMATICA to determine them. The resulting QNM frequencies provide an independent cross-check of the frequency-domain results. (ii) *Weak fit*: the frequencies are fixed to the values obtained in the frequency domain, while only amplitudes and phases are treated as fitting parameters. In this case, the fitting reduces to a linear regression problem [66], which we solve using the `LinearModelFit` function in MATHEMATICA. The extracted amplitudes then quantify the relative contribution of each QNM to the time-domain signal.

To assess the robustness of the extraction, we perform the fit over a sequence of time windows with varying start times and a fixed end time. If the waveform is well described by the chosen QNM ansatz, the fitted parameters exhibit a stable plateau and remain nearly constant over a range of start times [7, 8].

### III. QNM SPECTRUM

The emergence of an EP in the QNM spectrum is generally tied to the variation of at least two control parameters in the underlying non-Hermitian eigenvalue problem. In the EMS model, this requirement is naturally fulfilled by the coupling constant  $\alpha$  and the BH charge  $q$ . Motivated by this structure, in this section we carry out a frequency-domain search for EPs in the QNM spectrum. Our strategy is to fix  $\alpha$  and scan over  $q$  to track the evolution of neighboring QNM branches; if no coalescence is observed, we then adjust  $\alpha$  and repeat the scan. Following this procedure, for  $l = 2$  we find a pair of QNMs that coalesce at an EP located at  $\alpha = \alpha_{\text{EP}} \simeq 0.79040751953125$  and  $q = q_{\text{EP}} \simeq 1.0421911480$ .

We display the QNM spectrum at  $\alpha = \alpha_{\text{EP}}$  in Fig. 1. The left panel shows the trajectories of the QNM frequencies in the complex  $\omega$  plane as  $q$  is varied. The color bar indicates the value of  $q$ , with darker green corresponding to smaller  $q$ . The spectrum is organized into five distinct branches, two of which meet at the EP located at  $q = q_{\text{EP}}$ . These QNM branches can be further

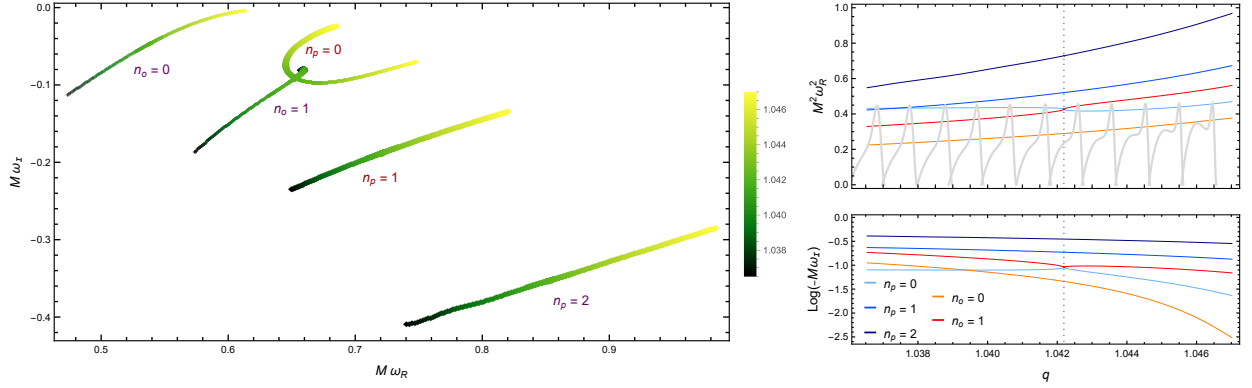


FIG. 1. QNM spectrum of the test scalar field at  $\alpha = \alpha_{\text{EP}}$  for  $l = 2$ . **Left:** Trajectories of QNM frequencies in the complex  $\omega$  plane as the BH charge  $q$  is varied. The color bar indicates the value of  $q$ . The spectrum is organized into five branches, two of which meet at an EP at  $q = q_{\text{EP}}$ . Near the EP, each of the two participating branches splits into an upper and a lower segment; the two upper (lower) segments recombine into the branch labeled by  $n_p = 0$  ( $n_o = 1$ ). Peak and off-peak modes are indexed by  $n_p$  and  $n_o$ , respectively. **Upper right:** Squared real part of the QNM frequencies,  $\omega_R^2$ , as a function of  $q$ . The gray dotted line marks  $q_{\text{EP}}$ , at which the real parts of the  $n_p = 0$  and  $n_o = 1$  branches cross. The panel also shows the effective potential  $V_{\text{eff}}$  for several representative values of  $q$ , with each curve aligned so that its highest peak corresponds to the selected  $q$ . As  $q$  increases,  $V_{\text{eff}}$  transitions from a single-peaked to a double-peaked structure. In the single-peak regime, peak and off-peak modes are distinguished by the location of  $\omega_R^2$ : the former lie close to the peak value of  $V_{\text{eff}}$ , whereas the latter take values appreciably below it. **Lower right:** Imaginary part of the QNM frequencies as a function of  $q$ . At  $q = q_{\text{EP}}$ , the imaginary parts of the  $n_p = 0$  and  $n_o = 1$  modes coincide.

classified into peak and off-peak modes, labeled by  $n_p$  and  $n_o$ , respectively [66]. A notable feature is that each of the two branches involved in the EP is naturally divided by the EP itself into an upper and a lower segment. The two upper segments recombine into the branch labeled by  $n_p = 0$ , whereas the two lower segments recombine into the branch labeled by  $n_o = 1$ . This branch reorganization reflects the local square-root structure of the non-Hermitian spectrum near the EP and is consistent with the mode switching or hysteresis behavior under parameter variation around an EP [36]. Hereafter, we refer to the two modes involved in the spectral coalescence, namely the  $n_p = 0$  and  $n_o = 1$  modes, as the EP modes.

The upper-right and lower-right panels of Fig. 1 show  $(M\omega_R)^2$  and  $\log(-M\omega_I)$  as functions of  $q$ , respectively, where  $\omega_R \equiv \text{Re}(\omega)$  and  $\omega_I \equiv \text{Im}(\omega)$ . The value of  $q_{\text{EP}}$  is marked by the gray dotted line. The upper-right panel shows that the squared real parts of the frequencies of the  $n_p = 0$  and  $n_o = 1$  branches cross at  $q = q_{\text{EP}}$ . It also displays the effective potential  $V_{\text{eff}}$  for several

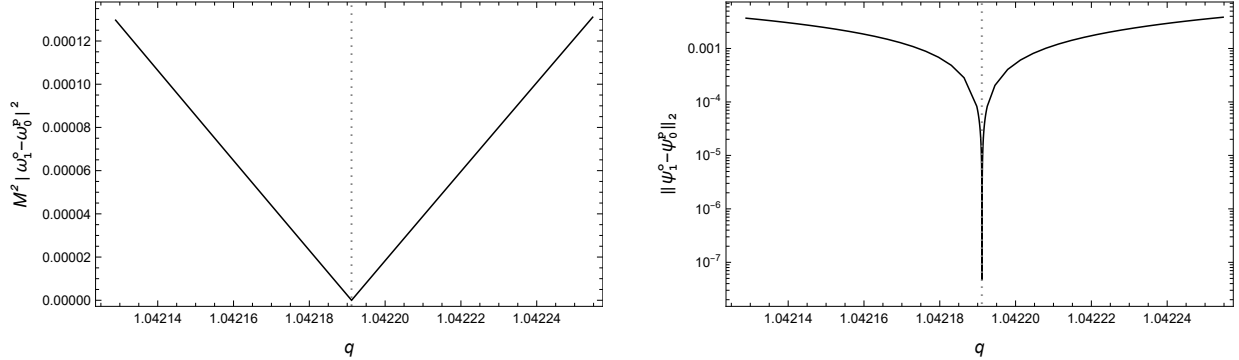


FIG. 2. Squared difference between the QNM frequencies  $\omega_0^p$  and  $\omega_1^o$  for the  $n_p = 0$  and  $n_o = 1$  modes (**Left**), and the  $L^2$  norm of the difference between the corresponding eigenfunctions  $\psi_1^o$  and  $\psi_0^p$  (**Right**), as functions of the BH charge  $q$ . In both panels, the gray dotted line marks the EP location at  $q = q_{\text{EP}}$ . As  $q$  approaches  $q_{\text{EP}}$ , the squared frequency difference decreases approximately linearly to an extremely small value, while the eigenfunction difference drops sharply, indicating the near coalescence of the two eigenfunctions. The simultaneous strong suppression of the eigenvalue and eigenfunction differences provides direct numerical evidence for the EP in the QNM spectrum.

representative values of  $q$ . For sufficiently small  $q$ , the effective potential has a single peak. The peak and off-peak modes labeled by  $n_p$  and  $n_o$  correspond to modes localized near the potential peak and appreciably below it, respectively.<sup>1</sup>

The peak and off-peak modes are ordered by their decay rates, with  $n_p = 0$  and  $n_o = 0$  corresponding to the least damped peak and off-peak modes, respectively. As shown in the lower-right panel, as  $q$  increases, the  $n_p = 0$  and  $n_o = 0$  modes undergo a fundamental-mode overtaking. Moreover, the imaginary parts of the frequencies of the  $n_p = 0$  and  $n_o = 1$  modes coincide at  $q = q_{\text{EP}}$ . At  $q = q_{\text{EP}}$ , the fundamental mode is the  $n_o = 0$  mode, while the EP modes appear as the lowest overtone. The lower-right panel also shows that branch reorganization occurs for the  $n_p = 0$  and  $n_o = 1$  modes in the neighborhood of the EP.

To further resolve the QNM behavior in the immediate vicinity of the EP, Fig. 2 shows the dependence on  $q$  of both the frequency splitting and the eigenfunction mismatch for the  $n_p = 0$  and  $n_o = 1$  modes. The left panel displays the squared frequency splitting,  $\delta\omega^2 \equiv |\omega_1^o - \omega_0^p|^2$ , as a function of  $q$  near  $q_{\text{EP}}$ , indicated by the gray dotted line. We observe a pronounced cusp at  $q = q_{\text{EP}}$ :  $\delta\omega^2$  decreases approximately linearly as  $q$  approaches  $q_{\text{EP}}$  from either side and increases again after passing through the EP. This behavior is characteristic of a second-order EP, where the local eigenvalue splitting scales as the square root of the control parameter, so that the squared

<sup>1</sup> The  $n_p = 2$  peak mode would reside near the potential peak for values of  $q$  smaller than those shown in Fig. 1.

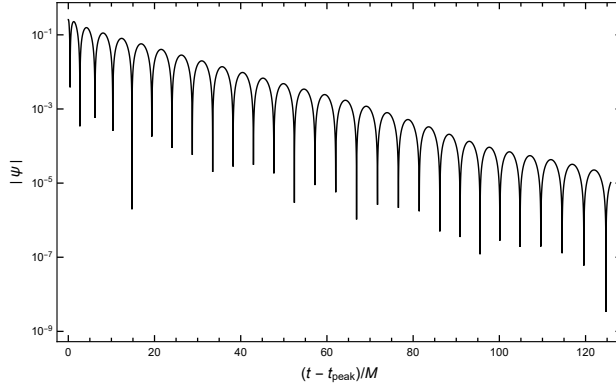


FIG. 3. Time-domain ringdown waveform  $\psi$  of the scalar field at  $\alpha = \alpha_{\text{EP}}$  and  $q = q_{\text{EP}}$ , plotted as a function of  $(t - t_{\text{peak}})/M$ . Here  $t_{\text{peak}}$  denotes the time at which the waveform amplitude reaches its maximum. The observer is located at  $r = 27.452M$ .

splitting becomes linear sufficiently close to the EP [36]. At  $q = q_{\text{EP}}$ , the numerical splitting does not vanish identically, but remains below our numerical tolerance of  $10^{-6}$ .

The right panel shows the corresponding  $L^2$  mismatch  $\|\psi_1^o - \psi_0^p\|_2$  between the two eigenfunctions  $\psi_1^o$  and  $\psi_0^p$ . As  $q$  approaches  $q_{\text{EP}}$ , this quantity drops sharply to an extremely small value, indicating that the two eigenfunctions become nearly indistinguishable. The simultaneous near vanishing of the eigenvalue splitting and the eigenfunction mismatch provides direct numerical evidence for the coalescence of both eigenvalues and eigenfunctions, which is the defining signature of an EP in a non-Hermitian QNM problem.

#### IV. QNM EXTRACTION

In this section, we extract QNMs from the time-domain waveform at  $\alpha = \alpha_{\text{EP}}$  and  $q = q_{\text{EP}}$ , where the frequency-domain analysis indicates the presence of an EP associated with the coalescence of two spectral branches. The waveform used in the extraction is shown in Fig. 3. We consider both the standard and EP ansatzes, given in Eqs. (17) and (18), respectively, to assess how the choice of ansatz affects the extracted frequencies and amplitudes. The extraction is performed using both the weak fit and strong fit schemes. In each case, we repeat the fit while varying the start time  $t_0$  over the interval  $(t_0 - t_{\text{peak}})/M \in [0, 130]$ . Here  $t_{\text{peak}}$  denotes the time at which the waveform amplitude reaches its maximum.

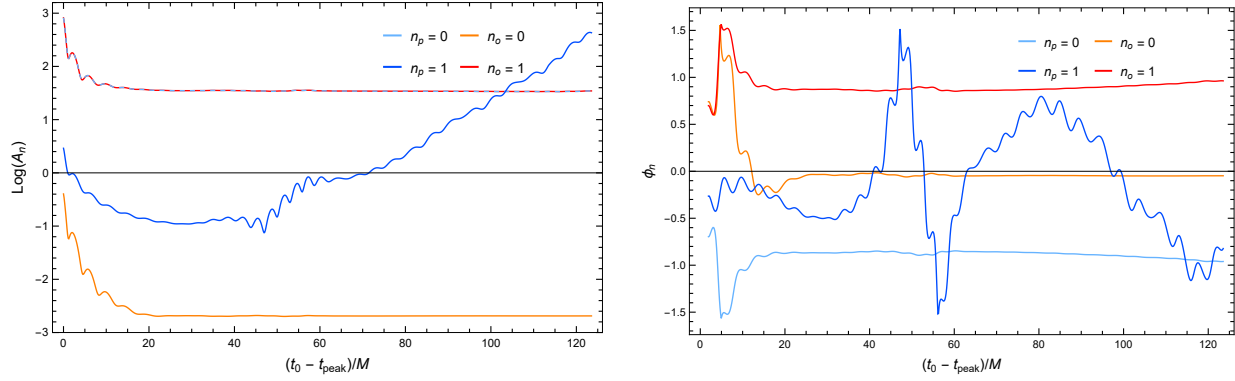


FIG. 4. Extracted amplitudes  $A_n$  (**Left**) and phases  $\phi_n$  (**Right**) obtained with the standard ansatz, shown as functions of the start time  $(t_0 - t_{\text{peak}})/M$ . The fit includes the four least damped modes, namely the  $n_p = 0, 1$  peak modes and the  $n_o = 0, 1$  off-peak modes, with frequencies fixed by the frequency-domain analysis. The two EP modes,  $n_p = 0$  and  $n_o = 1$ , have nearly equal amplitudes and dominate over the other fitted modes, while their phases are approximately opposite, indicating destructive interference between their contributions.

#### A. Weak Fit

We first apply the weak fit scheme based on the standard ansatz in Eq. (17) to extract the amplitudes and phases from the time-domain waveform. In this fit, we include the four least damped modes, namely the  $n_p = 0, 1$  peak modes and the  $n_o = 0, 1$  off-peak modes, with their frequencies fixed by the frequency-domain analysis. The left and right panels of Fig. 4 show the extracted amplitudes  $A_n$  and phases  $\phi_n$ , respectively, as functions of the start time  $(t_0 - t_{\text{peak}})/M$ . For three of the four modes, namely  $n_p = 0$ ,  $n_o = 0$ , and  $n_o = 1$ , both the amplitudes and phases approach clear plateaus for  $(t_0 - t_{\text{peak}})/M \gtrsim 20$ , indicating that these modes can be extracted reliably within this time window. By contrast, the  $n_p = 1$  mode exhibits a noticeably stronger dependence on  $t_0$ . Since it is the most strongly damped of the four modes, its extraction is feasible only over a relatively early interval, roughly  $20 \lesssim (t_0 - t_{\text{peak}})/M \lesssim 40$ , and is therefore less robust.

A particularly noteworthy feature is that the EP modes, namely the  $n_p = 0$  and  $n_o = 1$  modes, have nearly equal extracted amplitudes, both exceeding those of the other two modes by at least two orders of magnitude. This hierarchy indicates that the contribution from each individual EP mode is strongly enhanced in the ringdown signal. At the same time, these two dominant modes have approximately opposite phases, so that their contributions nearly cancel in the waveform. This pattern is consistent with recent analyses of ringdown near an EP, in which the resonant pair is strongly amplified while destructive interference between the dominant components suppresses

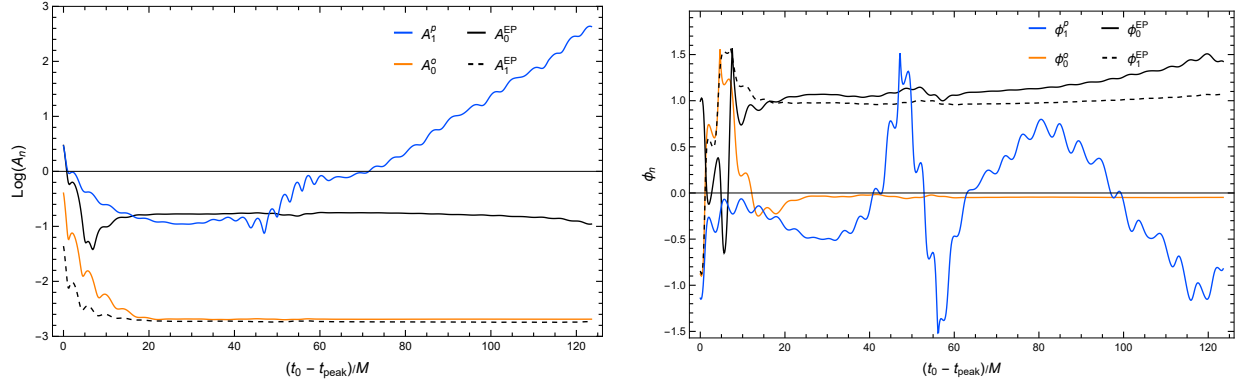


FIG. 5. Extracted amplitudes  $A_n$  (**Left**) and phases  $\phi_n$  (**Right**) obtained with the EP ansatz, shown as functions of the start time  $(t_0 - t_{\text{peak}})/M$ . The fit includes two nonresonant modes,  $n_o = 0$  and  $n_p = 1$ , together with the EP contribution, with frequencies fixed by the frequency-domain analysis. The EP contribution is decomposed into a time-independent term (solid black) and a term linear in time (dashed black). Their amplitudes are substantially smaller than the separate amplitudes of the EP modes obtained with the standard ansatz in Fig. 4, indicating that the EP ansatz provides a more economical description of the near-EP ringdown.

the net contribution to the waveform [49].

We next repeat the weak fit analysis using the EP ansatz, in which the two EP modes are replaced by a single EP contribution, while the nonresonant modes  $n_o = 0$  and  $n_p = 1$  are retained explicitly. The left and right panels of Fig. 5 show the extracted amplitudes and phases, respectively, as functions of the start time  $(t_0 - t_{\text{peak}})/M$ . A notable feature is that the EP contribution can be cleanly decomposed into a time-independent term and a term linear in time, both of which exhibit relatively stable plateaus over a broad fitting window. In contrast to the standard ansatz, where the two EP modes are treated separately and acquire very large extracted amplitudes, the EP ansatz absorbs their combined effect into a single resonant contribution with substantially smaller coefficients. This behavior indicates that the large amplitudes found in Fig. 4 arise primarily from forcing the near coalescing pair into two independent QNMs, whereas the EP ansatz captures the ringdown more economically in terms of the resonant structure near the EP. It is also worth noting that the time-independent and time-linear EP terms have almost identical phases, so that they add nearly in phase and together form a coherent resonant contribution. Altogether, Fig. 5 shows that the EP ansatz provides a more natural and stable description of the waveform in the near EP regime. Moreover, since the  $n_o = 0$  fundamental mode belongs to the off-peak family and is spectrally less stable, its contribution is suppressed relative to the EP contribution [66].

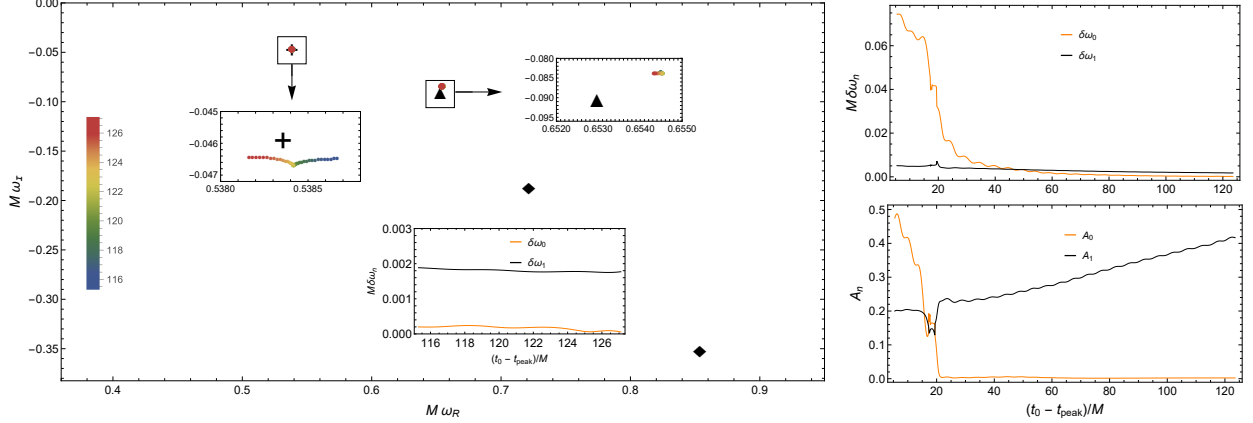


FIG. 6. Results of the strong fit using the standard ansatz with two modes included. **Left:** Extracted QNM frequencies in the complex  $\omega$  plane for different start times, shown as shaded dots. The color bar indicates the start time. The plus, triangle, and diamond markers denote the frequency-domain values of the fundamental mode, the EP modes, and the peak-mode overtones, respectively. The frequencies of the fundamental and EP modes can be extracted reliably. **Upper right:** Frequency deviations  $\delta\omega_0$  and  $\delta\omega_1$  for the fundamental and EP modes, plotted as functions of  $(t_0 - t_{\text{peak}})/M$ . The inset in the left panel shows that their minimum values are of order  $10^{-4}$  and  $10^{-3}$ , respectively. **Lower right:** Extracted amplitudes  $A_0$  and  $A_1$  for the fundamental and EP modes, plotted as functions of  $(t_0 - t_{\text{peak}})/M$ . For  $(t_0 - t_{\text{peak}})/M \gtrsim 20$ ,  $A_0$  remains approximately constant, whereas  $A_1$  increases nearly linearly with the start time.

## B. Strong Fit

In the strong fit scheme, we extract not only the amplitudes  $A_n$  and phases  $\phi_n$ , but also the frequencies  $\omega_n$  of the fitted modes. To assess the robustness of the extraction, we further introduce the frequency deviation,  $\delta\omega_n \equiv |\omega_n - \omega_{\text{FD}}^n|$ , which measures the difference between the frequency extracted from the time-domain fit and the corresponding frequency-domain value. In addition, for both the standard and the EP ansatzes, we consider fits involving either one mode or two modes.

We first consider the standard ansatz in Eq. (17). When only a single QNM is included in the fit, the only mode that can be extracted reliably is the one that asymptotically becomes the fundamental mode at late times. In this regime, the overtones, including the EP modes, have already decayed substantially, making their contributions to the waveform difficult to resolve.

The results of the two-mode fit with the standard ansatz are shown in Fig. 6. They show that the frequencies of both the fundamental and EP modes can be extracted reliably for  $(t_0 - t_{\text{peak}})/M \gtrsim 20$ . The left panel displays the extracted QNM frequencies in the complex  $\omega$  plane for  $115 \lesssim (t_0 - t_{\text{peak}})/M \lesssim 127$ , where the frequency deviations  $\delta\omega$  are close to their minimum values. The inset

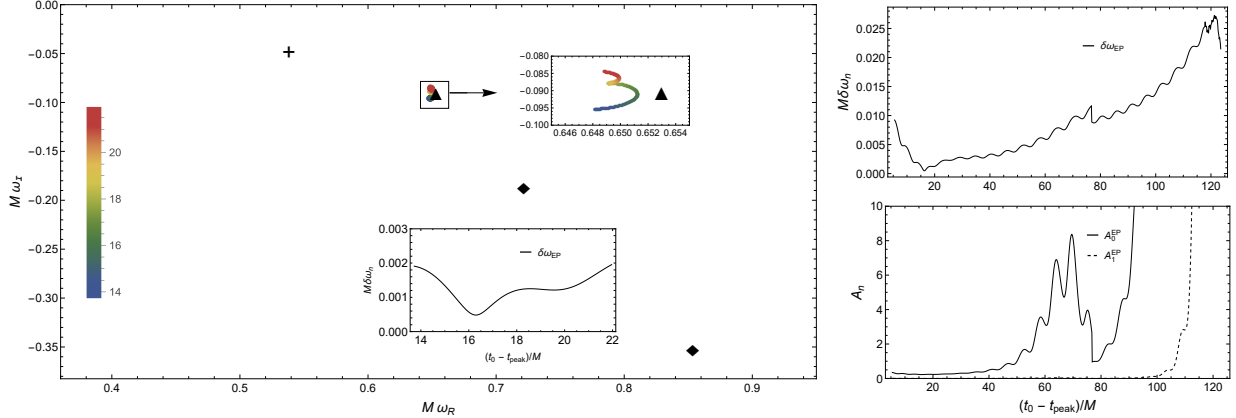


FIG. 7. Results of the strong fit obtained with the EP ansatz including only the EP terms. **Left:** Extracted frequencies in the complex  $\omega$  plane for  $14 \lesssim (t_0 - t_{\text{peak}})/M \lesssim 22$ . Throughout this interval, the extracted frequencies stay close to the frequency-domain value of  $\omega_{\text{EP}}$ . The inset shows that the frequency deviation  $\delta\omega_{\text{EP}}$  attains a minimum of order  $10^{-4}$  around  $(t_0 - t_{\text{peak}})/M \sim 16$ . The reference markers are the same as in Fig. 6. **Upper right:** Frequency deviation  $\delta\omega_{\text{EP}}$  as a function of the start time. **Lower right:** Extracted amplitudes  $A_0^{\text{EP}}$  and  $A_1^{\text{EP}}$  as functions of the start time. For  $(t_0 - t_{\text{peak}})/M \lesssim 40$ , both amplitudes remain approximately stable, indicating that the fit is reliable within this time window. At later times, they become increasingly unstable, accompanied by a growth in  $\delta\omega_{\text{EP}}$ .

further shows that the frequency deviation  $\delta\omega_0$  for the fundamental mode reaches a minimum of order  $10^{-4}$ , while the corresponding deviation  $\delta\omega_1$  for the EP mode reaches a minimum of order  $10^{-3}$ . More interestingly, the lower-right panel shows that, for  $(t_0 - t_{\text{peak}})/M \gtrsim 20$ , the extracted amplitude  $A_0$  of the fundamental mode remains approximately constant, whereas the extracted amplitude  $A_1$  of the EP mode increases almost linearly with the start time. This behavior is precisely what one would expect from the term linear in time appearing in the EP ansatz. In this sense, even when the waveform is fitted with the standard ansatz, the resulting fit tends to reproduce the characteristic structure encoded in the EP ansatz.

Fig. 7 shows the strong-fit results obtained with the EP ansatz including only the EP contribution. The lower-right panel displays the extracted amplitudes  $A_0^{\text{EP}}$  and  $A_1^{\text{EP}}$  as functions of the start time. For  $(t_0 - t_{\text{peak}})/M \lesssim 40$ , both amplitudes remain approximately stable, indicating that within this time window the waveform can be described reasonably well by the EP contribution alone. At later times, however, the amplitudes become increasingly unstable, while the frequency deviation  $\delta\omega_{\text{EP}}$  also grows. This behavior suggests that the EP ansatz containing only the EP terms is effective only over an early fitting window and becomes insufficient once the fundamental mode begins to dominate the waveform. The left panel shows the extracted frequencies in the com-

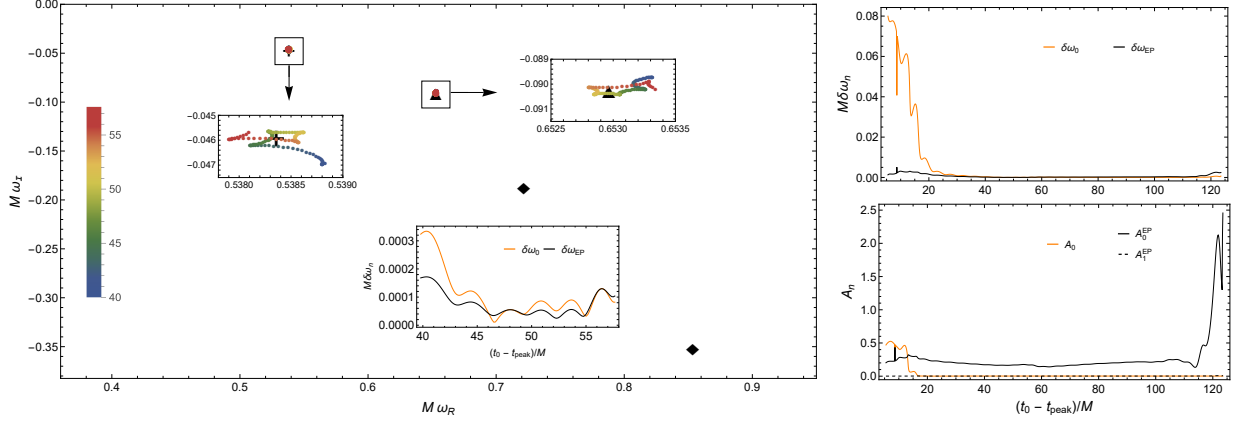


FIG. 8. Results of the strong fit obtained with the two-mode EP ansatz. **Left:** Extracted frequencies in the complex  $\omega$  plane as the start time varies over  $40 \lesssim (t_0 - t_{\text{peak}})/M \lesssim 60$ , with the color bar indicating  $(t_0 - t_{\text{peak}})/M$ . The reference markers are the same as in Fig. 6. The extracted frequencies are concentrated near the fundamental and EP modes. The inset shows that the minimum frequency deviations are of order  $10^{-5}$ . **Upper right:** Frequency deviations  $\delta\omega_0$  and  $\delta\omega_{\text{EP}}$  as functions of the start time. **Lower right:** Extracted amplitudes of the two contributions. The EP contribution is shown in black, with  $A_0^{\text{EP}}$  plotted as a solid line and  $A_1^{\text{EP}}$  as a dashed line. Compared with Fig. 7, the inclusion of the additional mode leads to a more stable extraction and yields broad plateaus for both contributions.

plex  $\omega$  plane as the start time varies over  $14 \lesssim (t_0 - t_{\text{peak}})/M \lesssim 22$ , indicating that the extracted frequencies remain close to the frequency-domain value of  $\omega_{\text{EP}}$ . The inset further shows that the frequency deviation  $\delta\omega_{\text{EP}}$  reaches a minimum of order  $10^{-4}$  around  $(t_0 - t_{\text{peak}})/M \sim 16$ .

We finally consider the two-mode strong fit based on the EP ansatz, in which the waveform is described by the EP contribution together with one additional QNM contribution. The results are shown in Fig. 8. The left panel shows the extracted frequencies in the complex  $\omega$  plane for  $40 \lesssim (t_0 - t_{\text{peak}})/M \lesssim 60$ , demonstrating that the extracted frequencies are concentrated near the fundamental and EP modes. The inset shows that the minimum frequency deviations are of order  $10^{-5}$ . Compared with the two-mode fit based on the standard ansatz, the minimum frequency deviations of the fundamental and EP modes are smaller by about one and two orders of magnitude, respectively. The lower-right panel shows the extracted amplitudes of the two contributions as functions of the start time, where the EP contribution is decomposed into  $A_0^{\text{EP}}$  and  $A_1^{\text{EP}}$ . In contrast to the single-mode fit in Fig. 7, the inclusion of the additional mode significantly improves the stability of the extraction and yields broad plateaus for both contributions. This indicates that, in this regime, the waveform is more accurately described by the combined contribution of the fundamental and EP modes.

## V. CONCLUSION

In this work, we investigated the QNM spectrum of a test massless scalar field on hairy BHs in the EMS theory. By exploring the parameter space spanned by the coupling constant  $\alpha$  and the BH charge  $q$ , we identified an EP in the frequency-domain spectrum at  $\alpha = \alpha_{\text{EP}}$  and  $q = q_{\text{EP}}$ , where two QNMs coalesce. Our analysis showed that this coalescence occurs not only at the level of the complex frequencies, but also at the level of the corresponding eigenfunctions. These results establish that EPs can arise in the scalar QNM spectra of hairy BHs and provide a concrete realization of non-Hermitian spectral degeneracies in BH perturbation theory.

We then investigated the time-domain signatures of the EP by extracting QNMs from the ring-down waveform at  $\alpha = \alpha_{\text{EP}}$  and  $q = q_{\text{EP}}$ . Using both weak fit and strong fit schemes, we compared the standard ansatz, based on the usual superposition of QNMs, with the EP ansatz, which incorporates the resonant contribution associated with the spectral degeneracy. In the weak fit analysis, with the frequencies fixed by the frequency-domain results, we found that the amplitudes of the two coalescing modes are much larger than those of the other modes, while destructive interference between their contributions strongly suppresses their net effect in the waveform. By contrast, the EP ansatz absorbs their combined effect into a single resonant contribution consisting of a time-independent term and a term linear in time, whose amplitudes are comparable to those of the other modes.

In the strong fit analysis, where the QNM frequencies are treated as fitting variables, the standard ansatz yields an amplitude that grows approximately linearly with the start time, mirroring the linear time dependence encoded in the EP ansatz. Moreover, the EP ansatz, especially in the two-mode fit, gives significantly smaller differences between the extracted frequencies and their frequency-domain counterparts. Together with the absence of the strong amplitude hierarchy found in the standard ansatz, these results indicate that the EP ansatz provides a more natural and robust description of ringdown signals near EPs.

Overall, our results show that EPs in QNM spectra are not merely features of the frequency-domain spectrum, but can also leave characteristic signatures in ringdown signals. This highlights the importance of the non-Hermitian spectral structure underlying BH perturbations and suggests that EP based descriptions may be useful for analyzing ringdown in systems with nearly degenerate QNMs. Possible extensions of the present work include the study of EPs in other perturbation sectors or in other hairy BH models, as well as a more systematic investigation of their implications for BH spectroscopy.

## ACKNOWLEDGMENTS

We are grateful to Yiqian Chen and Guangzhou Guo for helpful discussions and valuable comments. This work was supported in part by NSFC (Grant Nos. 12275183, 12275184, and 12175212) and by Development Fund Project of Shanghai University of Finance and Economics Zhejiang College for the Year 2024 (Grant No. 2024FZJJ02).

- 
- [1] Kostas D. Kokkotas and Bernd G. Schmidt. Quasinormal modes of stars and black holes. *Living Rev. Rel.*, 2:2, 1999. [arXiv:gr-qc/9909058](https://arxiv.org/abs/gr-qc/9909058), [doi:10.12942/lrr-1999-2](https://doi.org/10.12942/lrr-1999-2).
  - [2] Hans-Peter Nollert. TOPICAL REVIEW: Quasinormal modes: the characteristic ‘sound’ of black holes and neutron stars. *Class. Quant. Grav.*, 16:R159–R216, 1999. [doi:10.1088/0264-9381/16/12/201](https://doi.org/10.1088/0264-9381/16/12/201).
  - [3] Emanuele Berti, Vitor Cardoso, and Andrei O. Starinets. Quasinormal modes of black holes and black branes. *Class. Quant. Grav.*, 26:163001, 2009. [arXiv:0905.2975](https://arxiv.org/abs/0905.2975), [doi:10.1088/0264-9381/26/16/163001](https://doi.org/10.1088/0264-9381/26/16/163001).
  - [4] R. A. Konoplya and A. Zhidenko. Quasinormal modes of black holes: From astrophysics to string theory. *Rev. Mod. Phys.*, 83:793–836, 2011. [arXiv:1102.4014](https://arxiv.org/abs/1102.4014), [doi:10.1103/RevModPhys.83.793](https://doi.org/10.1103/RevModPhys.83.793).
  - [5] Emanuele Berti et al. Black hole spectroscopy: from theory to experiment. 5 2025. [arXiv:2505.23895](https://arxiv.org/abs/2505.23895).
  - [6] Matthew Giesler, Maximiliano Isi, Mark A. Scheel, and Saul Teukolsky. Black Hole Ringdown: The Importance of Overtones. *Phys. Rev. X*, 9(4):041060, 2019. [arXiv:1903.08284](https://arxiv.org/abs/1903.08284), [doi:10.1103/PhysRevX.9.041060](https://doi.org/10.1103/PhysRevX.9.041060).
  - [7] Vishal Baibhav, Mark Ho-Yeuk Cheung, Emanuele Berti, Vitor Cardoso, Gregorio Carullo, Roberto Cotesta, Walter Del Pozzo, and Francisco Duque. Agnostic black hole spectroscopy: Quasinormal mode content of numerical relativity waveforms and limits of validity of linear perturbation theory. *Phys. Rev. D*, 108(10):104020, 2023. [arXiv:2302.03050](https://arxiv.org/abs/2302.03050), [doi:10.1103/PhysRevD.108.104020](https://doi.org/10.1103/PhysRevD.108.104020).
  - [8] Kazuto Takahashi and Hayato Motohashi. Iterative extraction of overtones from black hole ringdown. *Class. Quant. Grav.*, 41(19):195023, 2024. [arXiv:2311.12762](https://arxiv.org/abs/2311.12762), [doi:10.1088/1361-6382/ad72c9](https://doi.org/10.1088/1361-6382/ad72c9).
  - [9] Ramy El-Ganainy, Konstantinos G. Makris, Mercedeh Khajavikhan, Ziad H. Musslimani, Stefan Rotter, and Demetrios N. Christodoulides. Non-Hermitian physics and PT symmetry. *Nature Phys.*, 14(1):11–19, 2018. [doi:10.1038/nphys4323](https://doi.org/10.1038/nphys4323).
  - [10] Emil J. Bergholtz, Jan Carl Budich, and Flore K. Kunst. Exceptional topology of non-Hermitian systems. *Rev. Mod. Phys.*, 93(1):015005, 2021. [arXiv:1912.10048](https://arxiv.org/abs/1912.10048), [doi:10.1103/revmodphys.93.015005](https://doi.org/10.1103/revmodphys.93.015005).
  - [11] Yuto Ashida, Zongping Gong, and Masahito Ueda. Non-Hermitian physics. *Adv. Phys.*, 69(3):249–435, 2021. [arXiv:2006.01837](https://arxiv.org/abs/2006.01837), [doi:10.1080/00018732.2021.1876991](https://doi.org/10.1080/00018732.2021.1876991).
  - [12] José Luis Jaramillo, Rodrigo Panosso Macedo, and Lamis Al Sheikh. Pseudospectrum and Black

- Hole Quasinormal Mode Instability. *Phys. Rev. X*, 11(3):031003, 2021. [arXiv:2004.06434](#), [doi:10.1103/PhysRevX.11.031003](#).
- [13] Mark Ho-Yeuk Cheung, Kyriakos Destounis, Rodrigo Panosso Macedo, Emanuele Berti, and Vitor Cardoso. Destabilizing the Fundamental Mode of Black Holes: The Elephant and the Flea. *Phys. Rev. Lett.*, 128(11):111103, 2022. [arXiv:2111.05415](#), [doi:10.1103/PhysRevLett.128.111103](#).
- [14] José Luis Jaramillo, Rodrigo Panosso Macedo, and Lamis Al Sheikh. Gravitational Wave Signatures of Black Hole Quasinormal Mode Instability. *Phys. Rev. Lett.*, 128(21):211102, 2022. [arXiv:2105.03451](#), [doi:10.1103/PhysRevLett.128.211102](#).
- [15] Li-Ming Cao, Jia-Ning Chen, Liang-Bi Wu, Libo Xie, and Yu-Sen Zhou. The pseudospectrum and spectrum (in)stability of quantum corrected Schwarzschild black hole. *Sci. China Phys. Mech. Astron.*, 67(10):100412, 2024. [arXiv:2401.09907](#), [doi:10.1007/s11433-024-2435-5](#).
- [16] A. Iannicari, A. J. Iovino, A. Kehagias, P. Pani, G. Perna, D. Perrone, and A. Riotto. Deciphering the Instability of the Black Hole Ringdown Quasinormal Spectrum. *Phys. Rev. Lett.*, 133(21):211401, 2024. [arXiv:2407.20144](#), [doi:10.1103/PhysRevLett.133.211401](#).
- [17] Yiqiu Yang, Zhan-Feng Mai, Run-Qiu Yang, Lijing Shao, and Emanuele Berti. Spectral instability of black holes: Relating the frequency domain to the time domain. *Phys. Rev. D*, 110(8):084018, 2024. [arXiv:2407.20131](#), [doi:10.1103/PhysRevD.110.084018](#).
- [18] Jia-Ning Chen, Liang-Bi Wu, and Zong-Kuan Guo. The pseudospectrum and transient of Kaluza–Klein black holes in Einstein–Gauss–Bonnet gravity. *Class. Quant. Grav.*, 41(23):235015, 2024. [arXiv:2407.03907](#), [doi:10.1088/1361-6382/ad89a1](#).
- [19] Rong-Gen Cai, Li-Ming Cao, Jia-Ning Chen, Zong-Kuan Guo, Liang-Bi Wu, and Yu-Sen Zhou. Pseudospectrum for the Kerr black hole with spin  $s=0$  case. *Phys. Rev. D*, 111(8):084011, 2025. [arXiv:2501.02522](#), [doi:10.1103/PhysRevD.111.084011](#).
- [20] Zhan-Feng Mai and Run-Qiu Yang. Butterfly in Spacetime: Inherent Instabilities in Stable Black Holes. 6 2025. [arXiv:2506.07562](#).
- [21] B. P. Abbott et al. Observation of Gravitational Waves from a Binary Black Hole Merger. *Phys. Rev. Lett.*, 116(6):061102, 2016. [arXiv:1602.03837](#), [doi:10.1103/PhysRevLett.116.061102](#).
- [22] B. P. Abbott et al. GW170817: Observation of Gravitational Waves from a Binary Neutron Star Inspiral. *Phys. Rev. Lett.*, 119(16):161101, 2017. [arXiv:1710.05832](#), [doi:10.1103/PhysRevLett.119.161101](#).
- [23] B. P. Abbott et al. Tests of General Relativity with GW170817. *Phys. Rev. Lett.*, 123(1):011102, 2019. [arXiv:1811.00364](#), [doi:10.1103/PhysRevLett.123.011102](#).
- [24] R. Abbott et al. Tests of general relativity with binary black holes from the second LIGO-Virgo gravitational-wave transient catalog. *Phys. Rev. D*, 103(12):122002, 2021. [arXiv:2010.14529](#), [doi:10.1103/PhysRevD.103.122002](#).
- [25] A. G. Abac et al. GWTC-4.0: An Introduction to Version 4.0 of the Gravitational-Wave Transient Catalog. *Astrophys. J. Lett.*, 995(1):L18, 2025. [arXiv:2508.18080](#), [doi:10.3847/2041-8213/ae0c06](#).

- [26] W. D. Heiss. Repulsion of Resonance States and Exceptional Points. 9 1999. [arXiv:quant-ph/9909047](#), [doi:10.1103/PhysRevE.61.929](#).
- [27] Shachar Klaiman, Nimrod Moiseyev, and Uwe Gunther. Visualization of Branch Points in PT-Symmetric Waveguides. *Phys. Rev. Lett.*, 101:080402, 2008. [arXiv:0802.2457](#), [doi:10.1103/PhysRevLett.101.080402](#).
- [28] Alexander I. Nesterov and F. Aceves de la Cruz. Complex magnetic monopoles, geometric phases and quantum evolution in vicinity of diabolic and exceptional points. *J. Phys. A*, 41:485304, 2008. [arXiv:0806.3720](#), [doi:10.1088/1751-8113/41/48/485304](#).
- [29] B. Dietz, H. L. Harney, O. N. Kirillov, M. Miski-Oglu, A. Richter, and F. Schaefer. Exceptional Points in a Microwave Billiard with Time-Reversal Invariance Violation. *Phys. Rev. Lett.*, 106:150403, 2011. [arXiv:1008.2623](#), [doi:10.1103/PhysRevLett.106.150403](#).
- [30] W. D. Heiss. The physics of exceptional points. *J. Phys. A*, 45:444016, 2012. [arXiv:1210.7536](#), [doi:10.1088/1751-8113/45/44/444016](#).
- [31] Jan Schnabel, Holger Cartarius, Jörg Main, Günter Wunner, and Walter Dieter Heiss.  $\mathcal{PT}$ -symmetric wave guide system with evidence of a third-order exceptional point. *Phys. Rev. A*, 95:053868, 2017. [arXiv:1703.05091](#), [doi:10.1103/PhysRevA.95.053868](#).
- [32] Qi Zhong, Mercedeh Khajavikhan, Demetrios Christodoulides, and Ramy El-Ganainy. Winding around Non-Hermitian Singularities: General Theory and Topological Features. 5 2018. [arXiv:1805.07620](#).
- [33] Akhil Kumar, Kater W. Murch, and Yogesh N. Joglekar. Maximal quantum entanglement at exceptional points via unitary and thermal dynamics. *Phys. Rev. A*, 105(1):012422, 2022. [arXiv:2109.07503](#), [doi:10.1103/PhysRevA.105.012422](#).
- [34] Jung-Wan Ryu, Jae-Ho Han, and Chang-Hwan Yi. A unified framework for exceptional point pairs in non-Hermitian two-level systems. 9 2025. [arXiv:2509.09129](#).
- [35] João Paulo Cavalcante, Maurício Richartz, and Bruno Carneiro da Cunha. Exceptional Point and Hysteresis in Perturbations of Kerr Black Holes. *Phys. Rev. Lett.*, 133(26):261401, 2024. [arXiv:2407.20850](#), [doi:10.1103/PhysRevLett.133.261401](#).
- [36] Yiqiu Yang, Emanuele Berti, and Nicola Franchini. Black Hole Quasinormal Mode Resonances. *Phys. Rev. Lett.*, 135(20):201401, 2025. [arXiv:2504.06072](#), [doi:10.1103/hfv8-n444](#).
- [37] Rodrigo Panosso Macedo, Takuya Katagiri, Kei-ichiro Kubota, and Hayato Motohashi. Exceptional Points and Resonance in Black Hole Ringdown. 12 2025. [arXiv:2512.02110](#).
- [38] João Paulo Cavalcante, Maurício Richartz, and Bruno Carneiro da Cunha. Massive scalar perturbations in Kerr black holes: Near extremal analysis. *Phys. Rev. D*, 110(12):124064, 2024. [arXiv:2408.13964](#), [doi:10.1103/PhysRevD.110.124064](#).
- [39] João Paulo Cavalcante, Maurício Richartz, and Bruno Carneiro da Cunha. Ergodic Hysteresis of the Kerr black hole spectrum. 11 2025. [arXiv:2511.16640](#).
- [40] Changkai Chen, Jiliang Jing, Zhoujian Cao, and Mengjie Wang. Complete quasinormal modes of type-D black holes. *Phys. Rev. D*, 112(10):103036, 2025. [arXiv:2506.14635](#), [doi:10.1103/f8m8-vr41](#).

- [41] Nao Nakamoto and Naritaka Oshita. Exceptional Lines and Excitation of (Nearly) Double-Pole Quasinormal Modes: A Semi-Analytic Study in the Nariai Black Hole. 1 2026. [arXiv:2601.00704](#).
- [42] Li-Ming Cao, Ming-Fei Ji, Liang-Bi Wu, and Yu-Sen Zhou. Exceptional line and pseudospectrum in black hole spectroscopy. 11 2025. [arXiv:2511.17067](#).
- [43] Liang-Bi Wu, Libo Xie, Li-Ming Cao, Ming-Fei Ji, and Yu-Sen Zhou. Quasinormal modes of Schwarzschild-de Sitter black holes in semi-open systems. *Sci. China Phys. Mech. Astron.*, 69(4):240415, 2026. [arXiv:2512.06903](#), [doi:10.1007/s11433-025-2912-y](#).
- [44] Hisashi Onozawa. A Detailed study of quasinormal frequencies of the Kerr black hole. *Phys. Rev. D*, 55:3593–3602, 1997. [arXiv:gr-qc/9610048](#), [doi:10.1103/PhysRevD.55.3593](#).
- [45] Oscar J. C. Dias, Mahdi Godazgar, Jorge E. Santos, Gregorio Carullo, Walter Del Pozzo, and Danny Laghi. Eigenvalue repulsions in the quasinormal spectra of the Kerr-Newman black hole. *Phys. Rev. D*, 105(8):084044, 2022. [arXiv:2109.13949](#), [doi:10.1103/PhysRevD.105.084044](#).
- [46] Oscar J. C. Dias, Mahdi Godazgar, and Jorge E. Santos. Eigenvalue repulsions and quasinormal mode spectra of Kerr-Newman: an extended study. *JHEP*, 07:076, 2022. [arXiv:2205.13072](#), [doi:10.1007/JHEP07\(2022\)076](#).
- [47] Alex Davey, Oscar J. C. Dias, and Jorge E. Santos. Scalar QNM spectra of Kerr and Reissner-Nordström revealed by eigenvalue repulsions in Kerr-Newman. *JHEP*, 12:101, 2023. [arXiv:2305.11216](#), [doi:10.1007/JHEP12\(2023\)101](#).
- [48] Hayato Motohashi. Resonant Excitation of Quasinormal Modes of Black Holes. *Phys. Rev. Lett.*, 134(14):141401, 2025. [arXiv:2407.15191](#), [doi:10.1103/PhysRevLett.134.141401](#).
- [49] Naritaka Oshita, Emanuele Berti, and Vitor Cardoso. Unstable Chords and Destructive Resonant Excitation of Black Hole Quasinormal Modes. *Phys. Rev. Lett.*, 135(3):031401, 2025. [arXiv:2503.21276](#), [doi:10.1103/ht2n-vvvh](#).
- [50] Rico K. L. Lo, Leart Sabani, and Vitor Cardoso. Quasinormal modes and excitation factors of Kerr black holes. *Phys. Rev. D*, 111(12):124002, 2025. [arXiv:2504.00084](#), [doi:10.1103/PhysRevD.111.124002](#).
- [51] Gregory B. Cook and Maxim Zolotarev. Gravitational perturbations of the Kerr geometry: High-accuracy study. *Phys. Rev. D*, 90(12):124021, 2014. [arXiv:1410.7698](#), [doi:10.1103/PhysRevD.90.124021](#).
- [52] Takuya Takahashi, Hayato Motohashi, and Kazufumi Takahashi. Resonance of black hole quasinormal modes in coupled systems. *Phys. Rev. D*, 112(6):064006, 2025. [arXiv:2505.03883](#), [doi:10.1103/59tb-2x9r](#).
- [53] Kei-ichiro Kubota and Hayato Motohashi. Resonance in black hole ringdown: Benchmarking quasinormal mode excitation and extraction. *Phys. Rev. D*, 113(4):043053, 2026. [arXiv:2509.06411](#), [doi:10.1103/pwyd-nv6v](#).
- [54] Carlos A.R. Herdeiro and Eugen Radu. Asymptotically flat black holes with scalar hair: a review. *Int. J. Mod. Phys. D*, 24(09):1542014, 2015. [arXiv:1504.08209](#), [doi:10.1142/S0218271815420146](#).
- [55] Carlos A.R. Herdeiro, Eugen Radu, Nicolas Sanchis-Gual, and José A. Font. Spontaneous Scalarization

- of Charged Black Holes. *Phys. Rev. Lett.*, 121(10):101102, 2018. [arXiv:1806.05190](#), [doi:10.1103/PhysRevLett.121.101102](#).
- [56] Yun Soo Myung and De-Cheng Zou. Quasinormal modes of scalarized black holes in the Einstein–Maxwell–Scalar theory. *Phys. Lett. B*, 790:400–407, 2019. [arXiv:1812.03604](#), [doi:10.1016/j.physletb.2019.01.046](#).
- [57] Pedro G. S. Fernandes, Carlos A. R. Herdeiro, Alexandre M. Pombo, Eugen Radu, and Nicolas Sanchis-Gual. Spontaneous Scalarisation of Charged Black Holes: Coupling Dependence and Dynamical Features. *Class. Quant. Grav.*, 36(13):134002, 2019. [Erratum: *Class.Quant.Grav.* 37, 049501 (2020)]. [arXiv:1902.05079](#), [doi:10.1088/1361-6382/ab23a1](#).
- [58] Pedro G.S. Fernandes, Carlos A.R. Herdeiro, Alexandre M. Pombo, Eugen Radu, and Nicolas Sanchis-Gual. Charged black holes with axionic-type couplings: Classes of solutions and dynamical scalarization. *Phys. Rev. D*, 100(8):084045, 2019. [arXiv:1908.00037](#), [doi:10.1103/PhysRevD.100.084045](#).
- [59] Jose Luis Blázquez-Salcedo, Carlos A.R. Herdeiro, Jutta Kunz, Alexandre M. Pombo, and Eugen Radu. Einstein-Maxwell-scalar black holes: the hot, the cold and the bald. *Phys. Lett. B*, 806:135493, 2020. [arXiv:2002.00963](#), [doi:10.1016/j.physletb.2020.135493](#).
- [60] Jose Luis Blázquez-Salcedo, Carlos A. R. Herdeiro, Sarah Kahlen, Jutta Kunz, Alexandre M. Pombo, and Eugen Radu. Quasinormal modes of hot, cold and bald Einstein–Maxwell-scalar black holes. *Eur. Phys. J. C*, 81(2):155, 2021. [arXiv:2008.11744](#), [doi:10.1140/epjc/s10052-021-08952-w](#).
- [61] Peng Wang, Houwen Wu, and Haitang Yang. Scalarized Einstein-Born-Infeld black holes. *Phys. Rev. D*, 103(10):104012, 2021. [arXiv:2012.01066](#), [doi:10.1103/PhysRevD.103.104012](#).
- [62] Guangzhou Guo, Peng Wang, Houwen Wu, and Haitang Yang. Scalarized Einstein–Maxwell-scalar black holes in anti-de Sitter spacetime. *Eur. Phys. J. C*, 81(10):864, 2021. [arXiv:2102.04015](#), [doi:10.1140/epjc/s10052-021-09614-7](#).
- [63] Guangzhou Guo, Peng Wang, Houwen Wu, and Haitang Yang. Quasinormal modes of black holes with multiple photon spheres. *JHEP*, 06:060, 2022. [arXiv:2112.14133](#), [doi:10.1007/JHEP06\(2022\)060](#).
- [64] Zakaria Belkhadria and Alexandre M. Pombo. Mixed scalarization of charged black holes: From spontaneous to nonlinear scalarization. *Phys. Rev. D*, 110(4):044014, 2024. [arXiv:2311.15850](#), [doi:10.1103/PhysRevD.110.044014](#).
- [65] Marco Melis, Fabrizio Corelli, Robin Croft, and Paolo Pani. Black hole spectroscopy and nonlinear echoes in Einstein-Maxwell-scalar theory. *Phys. Rev. D*, 111(6):064072, 2025. [arXiv:2412.14259](#), [doi:10.1103/PhysRevD.111.064072](#).
- [66] Peng Wang and Tianshu Wu. Coexistence of spectrally stable and unstable modes in black hole ringdowns. 2025. [arXiv:2510.12135](#).
- [67] Cheng-Yong Zhang, Qian Chen, Yunqi Liu, Wen-Kun Luo, Yu Tian, and Bin Wang. Critical Phenomena in Dynamical Scalarization of Charged Black Holes. *Phys. Rev. Lett.*, 128(16):161105, 2022. [arXiv:2112.07455](#), [doi:10.1103/PhysRevLett.128.161105](#).
- [68] Cheng-Yong Zhang, Qian Chen, Yuxuan Liu, Yu Tian, Bin Wang, and Hongbao Zhang. Nonlinear

- self-interaction induced black hole bomb. *Phys. Rev. D*, 110(4):L041505, 2024. [arXiv:2309.05045](#), [doi:10.1103/PhysRevD.110.L041505](#).
- [69] Yu-Peng Zhang, Si-Jiang Yang, Shao-Wen Wei, Wen-Di Guo, and Yu-Xiao Liu. Dynamical formation of axionic hair around a charged black hole. *Phys. Rev. D*, 111(10):104005, 2025. [arXiv:2412.13481](#), [doi:10.1103/PhysRevD.111.104005](#).
- [70] Sebastian Garcia-Saenz, Guangzhou Guo, Peng Wang, and Xinmiao Wang. Black hole accretion of scalar clouds with spontaneous symmetry breaking. *Phys. Rev. D*, 110(12):124045, 2024. [arXiv:2409.13184](#), [doi:10.1103/PhysRevD.110.124045](#).
- [71] Guangzhou Guo, Peng Wang, and Yu-Peng Zhang. Nonlinear stability of black holes with a stable light ring. *Phys. Rev. D*, 112(8):084023, 2025. [arXiv:2403.02089](#), [doi:10.1103/xlsl-8dtq](#).
- [72] Cheng-Yong Zhang, Zehong Zhang, and Ruifeng Zheng. Extraction of energy from a black hole in Einstein-Maxwell-scalar theory. *Sci. China Phys. Mech. Astron.*, 68(5):250411, 2025. [arXiv:2503.08315](#), [doi:10.1007/s11433-024-2607-1](#).
- [73] Sebastian Garcia-Saenz, Guangzhou Guo, Peng Wang, and Xinmiao Wang. Hairless black hole by superradiance. *JHEP*, 08:093, 2025. [arXiv:2502.18003](#), [doi:10.1007/JHEP08\(2025\)093](#).
- [74] Bo-Wen Qin and Yu-Peng Zhang. Effects of nonlinear interactions on the superradiant instability of charged black holes. 2 2026. [arXiv:2602.05268](#).
- [75] Qingyu Gan, Peng Wang, Houwen Wu, and Haitang Yang. Photon ring and observational appearance of a hairy black hole. *Phys. Rev. D*, 104(4):044049, 2021. [arXiv:2105.11770](#), [doi:10.1103/PhysRevD.104.044049](#).
- [76] Guangzhou Guo, Peng Wang, Houwen Wu, and Haitang Yang. Scalarized Kerr-Newman black holes. *JHEP*, 10:076, 2023. [arXiv:2307.12210](#), [doi:10.1007/JHEP10\(2023\)076](#).
- [77] Qingyu Gan, Peng Wang, Houwen Wu, and Haitang Yang. Photon spheres and spherical accretion image of a hairy black hole. *Phys. Rev. D*, 104(2):024003, 2021. [arXiv:2104.08703](#), [doi:10.1103/PhysRevD.104.024003](#).
- [78] Guangzhou Guo, Xin Jiang, Peng Wang, and Houwen Wu. Gravitational lensing by black holes with multiple photon spheres. *Phys. Rev. D*, 105(12):124064, 2022. [arXiv:2204.13948](#), [doi:10.1103/PhysRevD.105.124064](#).
- [79] Yiqian Chen, Guangzhou Guo, Peng Wang, Houwen Wu, and Haitang Yang. Appearance of an infalling star in black holes with multiple photon spheres. *Sci. China Phys. Mech. Astron.*, 65(12):120412, 2022. [arXiv:2206.13705](#), [doi:10.1007/s11433-022-1986-x](#).
- [80] Yiqian Chen, Peng Wang, and Haitang Yang. Interferometric signatures of black holes with multiple photon spheres. *Phys. Rev. D*, 110(4):044020, 2024. [arXiv:2312.10304](#), [doi:10.1103/PhysRevD.110.044020](#).
- [81] Yiqian Chen, Peng Wang, and Haitang Yang. Observations of orbiting hot spots around scalarized Reissner–Nordström black holes. *Eur. Phys. J. C*, 84(3):270, 2024. [arXiv:2401.10905](#), [doi:10.1140/epjc/s10052-024-12635-7](#).